AIMS Materials Science, 13(5): 882–896.
DOI: 10.3934/matersci.2026041
Received: 24 August 2026
Revised: 19 September 2026
Accepted: 23 September 2026
Published: 08 October 2026

https://www.aimspress.com/journal/Materials

Research article

Effect of multidirectional rolling on texture evolution and sputtering film deposition in Ti targets

Kewen Zhao[1], Longzhen Zhang[1,2,*], Zhipeng Song[1], Hongjun Yuan[3], Wei Zhang[1], Juanjuan Wang[1], Junbao Guo[1], Chengyu Hu[3], Gequan Hu[3], Xiaochao Wu[2], Qingkui Li[2] and Jilin He[2]

[1] School of Materials Science and Engineering, Zhongyuan Critical Metals Laboratory, Zhengzhou University, Zhengzhou 450001, China
[2] The National Key Laboratory of Special Rare Metal Materials, Zhengzhou University, Zhengzhou 450001, China
[3] Ningxia Horizontal Titanium Industry Co. Ltd, Ningxia 753000, China

* **Correspondence:** Email: zlz@zzu.edu.cn; Tel: +86-176-980-602-50.

Abstract: High-purity titanium (Ti) sputtering targets are essential for the fabrication of advanced Ti-based thin films with excellent electrical conductivity, adhesion, and diffusion barrier properties. Moreover, the important role of Ti films as functional layers in integrated circuits makes Ti targets indispensable sputtering materials in advanced manufacturing. The grain size and {0001} basal texture of Ti targets are crucial factors determining sputtering performance and film quality. In this study, high-purity Ti ingots (99.9994 wt.%) were processed via multi-directional rolling at 0°, 45°, and 90° combined with annealing. The sample rolled at 45° achieved the finest grains with an average grain size of 15.77 μm, which is much lower than the 30 μm standard for commercial titanium targets. Additionally, the rolling strategy effectively regulated the {0001} basal texture, with the <0001>// fraction decreasing from 42.7% (unidirectional rolling) to 16.7% (90° cross-rolling). In addition, this work revealed the correlations among target grain size, {0001} texture evolution, and deposited-film properties. Notably, the 45°-rolled annealed target achieved the maximum film deposition rate of 22.02 nm/min, exceeding the value of 17.70 nm/min for the unidirectionally rolled target. The findings provide valuable guidance for the preparation and performance optimization of high-purity Ti sputtering targets.

Keywords: titanium target; multi-directional rolling; texture; magnetron sputtering

1. Introduction

Titanium (Ti) targets serve as the core source material for fabricating high-purity Ti thin films via physical vapor deposition (PVD) technology, and hold significant application value in electronic information [1–4]. As semiconductor integrated circuits continue to evolve toward smaller feature sizes, higher integration density, and greater reliability, Ti thin films employed as interconnection layers and diffusion barrier layers impose more stringent requirements on deposition rate, thickness uniformity, particle contamination control, surface roughness, electrical resistivity, and adhesion [5–7]. Apart from target microstructure, impurity content and sputtering parameters strongly affect film properties. Impurities trigger arcing and particle defects, while process variables adjust deposition rate and surface morphology [8–10]. These film properties are largely governed by the intrinsic microstructure of Ti targets, including grain size, texture characteristics, and grain uniformity.

Numerous studies have verified that impurity content of Ti targets and sputtering processes influence film properties. For instance, Liu [8] demonstrated that the higher the purity of the Ti target, the fewer impurities in the prepared Ti film, the better its density and uniformity, as well as the lower surface roughness and electrical resistivity. Wu [9] investigated the tailoring of Ti film properties by adjusting peak and average power in high-power pulsed magnetron sputtering. Higher peak power reduced the deposition rate and refined grains, whereas higher average power promoted grain coarsening, (002) preferred orientation, and tensile stress. Conversely, the grain size, grain-size uniformity, and texture distribution of targets decisively influence the properties of sputtered films. Zhu [11] reported that hot extrusion refined the grains of Mo targets, rendering the microstructure finer and more uniform with distinct preferred orientation texture, which is highly beneficial for reducing the surface roughness and improving the crystalline quality of sputtered molybdenum thin films. Zhang [12] focused on Ti targets and found that microstructural uniformity directly affects film deposition rate and surface quality, with fine-grained Ti targets producing films with fewer surface particles, lower roughness, and better electrical resistivity. Song [13] showed that texture-controlled rolling and annealing form specific preferred orientations in Al targets. Low-temperature rolling produces {001} grains, while higher temperature generates cube texture, enhancing film uniformity and conductivity. Nevertheless, systematic research focusing on the synergistic regulation of grain refinement and texture optimization for high-performance Ti sputtering targets is still insufficient and needs further exploration [14].

To tackle the aforementioned issues, multi-directional rolling was employed in this work to refine grains, whereby 90°, 45° and unidirectional rolling routes were adopted to regulate the grain orientation and texture evolution of Ti targets. On this basis, the influences of rolling direction and rotation angle on grain refinement, microstructural homogeneity, texture characteristics of Ti targets, and the performance of the corresponding sputtered thin films were systematically analyzed, providing a scientific basis for optimizing the fabrication process of high-purity Ti targets.

2. Materials and methods

2.1. Chemicals and materials

The experimental raw material was a high-purity Ti ingot with a purity of 99.9994 wt.%, purchased from Beijing Yanbang New Material Co., Ltd., which conforms to the 5N-grade Ti target standard specified in the Chinese national standard YS/T 893-2013.

2.2. Target preparation process

The experimental raw material was a Ti plate with dimensions of 60 × 30 × 20 mm (TD × RD × ND). TD, RD, and ND stand for transverse, rolling, and thickness directions, respectively. The Ti plate surface oxide layer was removed by mechanical grinding, after which it was rolled in a twin-roll rolling mill. The rolling direction was kept constant during rolling, with a reduction of 0.5 mm per pass, a cumulative deformation of 80%, and a roll rotating speed of 300 r/min. The as-rolled sample with a final thickness of 4 mm was reserved for annealing and denoted as the unidirectionally rolled sample.

To prepare Ti targets with different rolling directions, the raw material was cut into specimens of 30 × 30 × 20 mm. The 45° rolled sample was obtained by rotating the specimen clockwise by 45° relative to the rolling direction of the previous pass before each subsequent rolling pass, and this procedure was repeated until the preset deformation was achieved. The 90° rolled sample was prepared by rotating the specimen clockwise by 90° before each subsequent pass after the first pass until the cumulative deformation reached 80%. The rest of the experimental procedure was consistent with that of the unidirectionally rolled sample.

For annealing, the vacuum was pumped to approximately 1.0×10^{-2} Pa, and high-purity argon was introduced as a protective atmosphere. A heating profile was applied at a heating rate of 5 ℃/min to 600 ℃, followed by holding for 1 h, and the samples were then furnace-cooled to room temperature before being taken out.

Subsequently, the samples were sequentially processed by wire electrical discharge machining (WEDM), mechanical grinding, and polishing to produce high-quality sputtering targets with dimensions of φ50.8 × 4 mm.

2.3. Thin film deposition process

Glass substrates were ultrasonically cleaned in deionized water, acetone, and anhydrous ethanol in sequence for 15 min each, then blow-dried with high-purity nitrogen and vacuum-sealed for subsequent experiments. The Ti target and substrates were placed into the multifunctional magnetron sputtering system. The target–substrate distance was adjusted to 75 mm, and the chamber was closed and evacuated to below 8×10^{-4} Pa. Argon gas was then introduced at a flow rate of 60 sccm, the deposition pressure was regulated to 0.5 Pa, and the sputtering power was set to 120 W, followed by pre-sputtering for 10 min. The substrate stage was set to rotate at 20 r/min, the substrate shutter was opened, and sputtering deposition was carried out for 20 min. Upon completion of thin film deposition, the chamber was cooled to room temperature. The thin film samples and target were then removed, and the experimental equipment was shut down.

2.4. Characterization

All samples were subjected to X-ray diffraction (XRD) analysis using a Shimadzu 6100 diffractometer (Japan) with Cu-Kα radiation. The measurements were performed over a 2θ range of 10°–90°, at an accelerating voltage of 45 kV and an accelerating current of 40 mA; scanning electron microscopy (SEM) characterization was conducted on a Sigma 300 microscope (Zeiss, Germany), with an accelerating voltage ranging from 0.02 to 30 kV and a magnification range of 50× to 100000×; electron backscatter diffraction (EBSD) tests were carried out using a Symmetry S2 EBSD detector integrated with a Ge mini300 scanning electron microscope, at an accelerating voltage of 20 kV. Three non-overlapping EBSD measurement regions were acquired for each sample. The acquired EBSD data were analyzed using the Oxford AZtecCrystal software; atomic force microscopy (AFM) was employed to characterize the surface morphology and surface roughness of the pure Ti thin films. The tests were performed on a Dimension Icon microscope (Bruker, Germany) with a scanning area of 20 × 20 μm, and the obtained data were processed and analyzed using the NanoScope Analysis software.

3. Results

3.1. Microstructure and texture of as-rolled samples

XRD patterns were recorded to investigate the texture evolution of samples with different rolling directions, as presented in Figure 1. The 90° rolled sample exhibits two dominant texture peaks, corresponding to the (0002) and (10$\bar{1}$1) crystal planes, where the intensity of the (0002) peak is slightly higher than that of the (10$\bar{1}$1) peak, while the diffraction peaks of other crystal planes are relatively weak. Compared with the unidirectionally rolled sample, the relative intensity of the (10$\bar{1}$3) peak decreases for the 90° rolled sample, and the overall texture variation is minor. As the rotation angle per rolling pass decreases, the relative intensities of the (0002) and (10$\bar{1}$1) peaks are weakened and become nearly equal, indicating that the 45° rolled sample possesses weaker texture and more homogeneous microstructure.

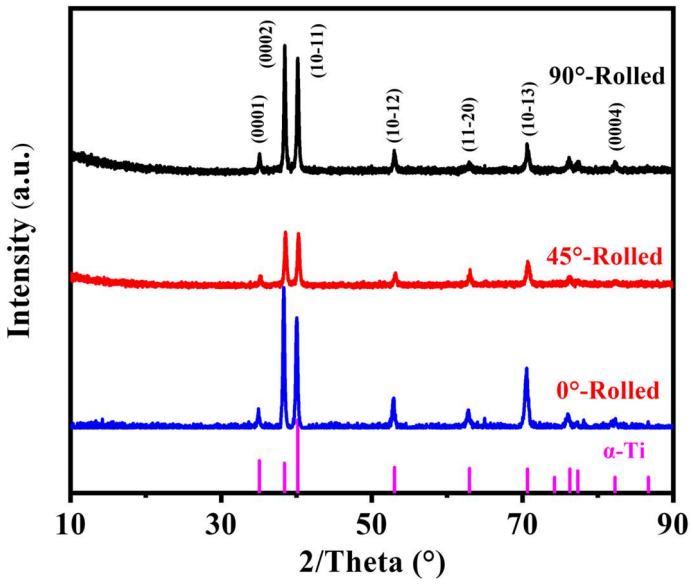


Figure 1. XRD patterns of samples with different rolling directions.

The pole figures of samples with different rolling directions are presented in Figure 2a–c, where RD and TD represent the major elongation direction and minor elongation direction during the initial rolling pass, respectively. Figure 2c shows the unidirectionally rolled sample, which exhibits a typical basal double-peak texture. This texture is a common orientation distribution in hexagonal close-packed (HCP) metals after unidirectional rolling. Specifically, the normal direction of the basal {0001} plane is not strictly parallel to the sample ND but presents a characteristic deflection. The two symmetric texture peaks deviate from the TD by approximately 45°, forming a double-peak distribution pattern. The pole density is 15.89, reflecting the high concentration of grain orientations during unidirectional rolling. With the reduction of the rotation angle per rolling pass, the fragmentation degree of the as-cast microstructure is gradually enhanced, and the grain orientations become more homogeneous and randomized. Consequently, the basal double-peak texture starts to spread toward the RD direction with new texture components generated, and the pole density decreases progressively, as illustrated in Figure 2a,b.

Figure 2d–o displays the band contrast (BC) maps, grain size distribution maps, kernel average misorientation (KAM) maps, and inverse pole figure (IPF) maps of targets with different rolling modes corresponding to the 90° cross-rolled sample, 45° cross-rolled sample, and unidirectionally rolled sample, respectively. The small grains in the unidirectionally rolled sample are mostly red or green and relatively few are blue, indicating that the small grains after rolling tend to form the orientations of <0001>//ND and <11$\bar{2}$0>//ND. Grains of different sizes exhibit a broader spread of transitional orientations, indicating that the orientation distribution becomes more heterogeneous after rolling. These observations provide direct information on the grain orientation distribution but do not by themselves establish a specific deformation mechanism, as twinning causes texture randomization

It can be seen from Figure 2g,h that as the rotation angle per rolling pass decreases from 90° to 45°, the fragmentation degree of the as-cast microstructure is gradually enhanced, and the grain size is reduced accordingly. However, the grains are dominated by red and green colors, suggesting that the orientation of the samples after multi-directional rolling changes slightly and remains dominated by <0001>//ND and <11$\bar{2}$0>//ND. The blue grains in the 45° rolled sample increase slightly, indicating a more uniform microstructure. Compared with the unidirectionally rolled sample, which presents coarse grains and extremely poor grain uniformity, the multi-directionally rolled samples have no incompletely fragmented large grains or unidirectionally elongated grains. Nevertheless, obvious differences in partial grain sizes can still be observed in the 90° rolled sample, while the 45° rolled sample exhibits more uniform grain sizes. As shown in Figure 2g–i, the average grain sizes of the samples with different rolling directions are 4.30, 3.76, and 2.28 μm, and the maximum grain sizes are 34.40, 13.93, and 8.14 μm, respectively. About 150 grains were counted for grain-size statistics.

The KAM maps of samples with different rolling directions are displayed in Figure 2j–l. The KAM values of the 90° rolled sample, 45° rolled sample, and unidirectionally rolled sample are 1.66°, 1.75°, and 1.95°, respectively. These results indicate that rolling introduces considerable local strain/lattice distortion, which is mainly concentrated within the grains. Figure 2m–o show the misorientation angle distribution maps and rotation axis distribution maps of the samples with different rolling directions. It can be observed that all three samples present a single misorientation angle peak at approximately 5°. According to the rotation axis distribution maps, the rotation axis is identified as <0001>, which is barely affected by the rolling direction.

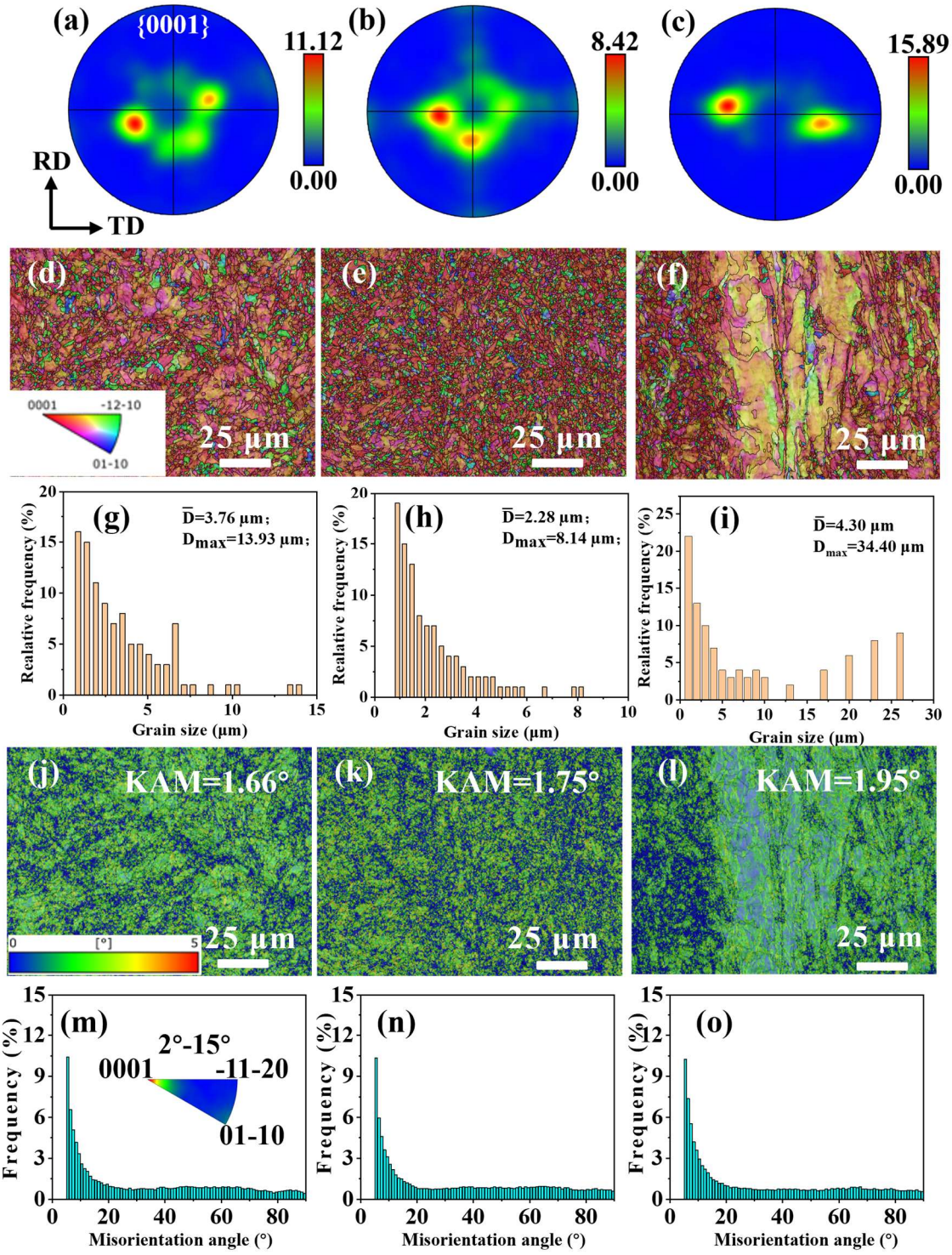


Figure 2. Pole figures, BC maps, grain size distribution maps, KAM maps, and IPF maps of rolled targets:(a, d, g, j, m) 90° rolled target; (b, e, h, k, n) 45° rolled target; and (c, f, i, l, o) 0° rolled target.

3.2. Microstructure and texture of annealed samples

The XRD patterns of the annealed samples with different rolling modes are presented in Figure 3a. After annealing at 600 ℃ for 1 h, the unidirectionally rolled sample exhibits three dominant diffraction

peaks corresponding to the (0002), (10$\bar{1}$1), and (10$\bar{1}$3) crystal planes. Among them, the peak intensity of the (0002) plane is significantly higher than those of the (10$\bar{1}$1) and (10$\bar{1}$3) planes, indicating the highest content of the (0002) plane in the unidirectionally rolled annealed sample, with similar peak intensities observed for the (10$\bar{1}$1) and (10$\bar{1}$3) planes. With the variation of rolling modes, the peak intensity of the (10$\bar{1}$1) plane increases notably and becomes close to that of the (0002) plane in the 45° and 90° cross-rolled annealed samples, while the peak intensity of the (10$\bar{1}$3) plane decreases. This suggests that the (0002) and (10$\bar{1}$1) planes are relatively abundant in the two cross-rolled samples.

Figure 3b shows that the 45° and 90° targets have broader XRD reflections than the unidirectionally rolled target, together with a shift toward higher 2θ. The (0002) FWHM (full width at half maximum) increases from [0.14 ± 0.01]° to [0.23 ± 0.02]° and [0.27 ± 0.02]°, indicating higher residual microstrain and reduced average interplanar spacing after multidirectional rolling.

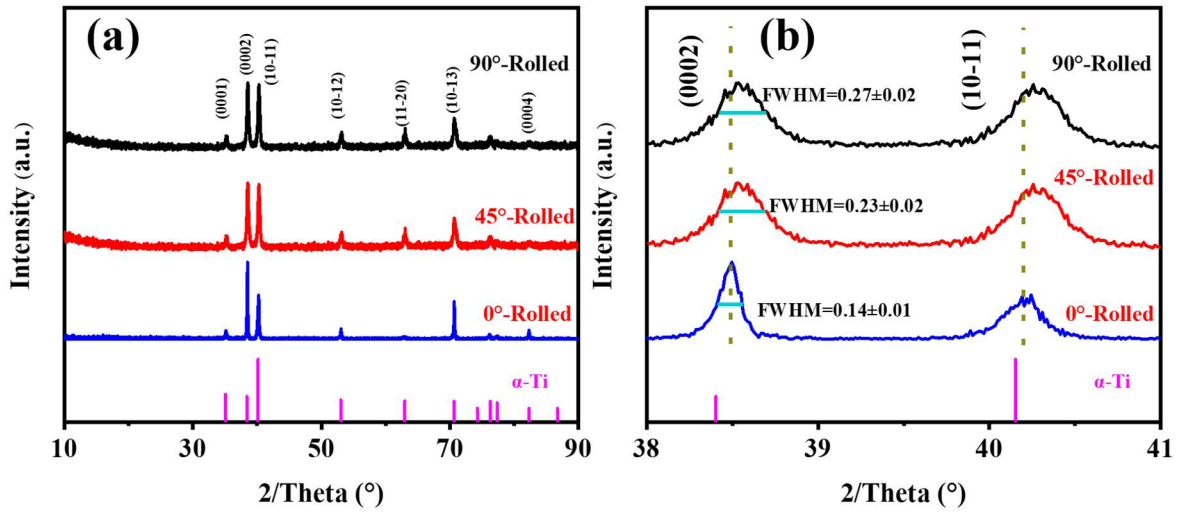


Figure 3. (a) XRD patterns of annealed targets with different rolling directions; and (b) magnified view of the selected XRD peaks.

To further investigate the texture evolution of annealed samples with different rolling directions, pole figure characterization was carried out, and the results are presented in Figure 4a–c. After annealing, the texture of the 90° rolled sample differs from that of the unidirectionally rolled annealed target. The basal double-peak texture in the {0001} pole figure becomes indistinct, the texture begins to disperse, and new texture peaks emerge along the RD direction, accompanied by a reduced pole density (the pole density of the unidirectionally rolled annealed sample is 12.91). This is because changing the rolling direction prevents grains from deforming along a single orientation, leading to gradual randomization of grain orientations during rolling. The newly recrystallized grains formed after annealing inherit the random orientation characteristics of the as-rolled grains. When the rolling rotation angle is reduced to 45°, the grain orientations of the as-rolled sample become more randomized, and this random feature is retained after annealing. The overall texture exhibits a ring-like distribution, with the pole density further decreasing to 6.96.

The orientation distribution function (ODF) maps of annealed samples with different rolling directions are displayed in Figure 4d,f, and h. The annealed 90° rolled sample mainly contains three types of textures: {0001}<11$\bar{2}$0> texture, <10$\bar{1}$0>//RD texture, and <11$\bar{2}$0>//RD texture, with a weak overall texture intensity. This is attributed to the diversified grain orientations introduced by varying

rolling directions during deformation, which are preserved after annealing. The reduced distribution probability of grains at specific orientations lowers the overall texture intensity. For the annealed 45° rolled sample, the dominant texture is {0001}<11$\bar{2}$0>texture, while the intensities of <10$\bar{1}$0>//RD and <11$\bar{2}$0>//RD textures are significantly weakened, resulting in a slight increase in the overall texture intensity. In contrast, the unidirectionally rolled sample presents a single {0001} texture after annealing. These results demonstrate that changing the rolling direction homogenizes the grain orientation distribution but delays the texture evolution process.

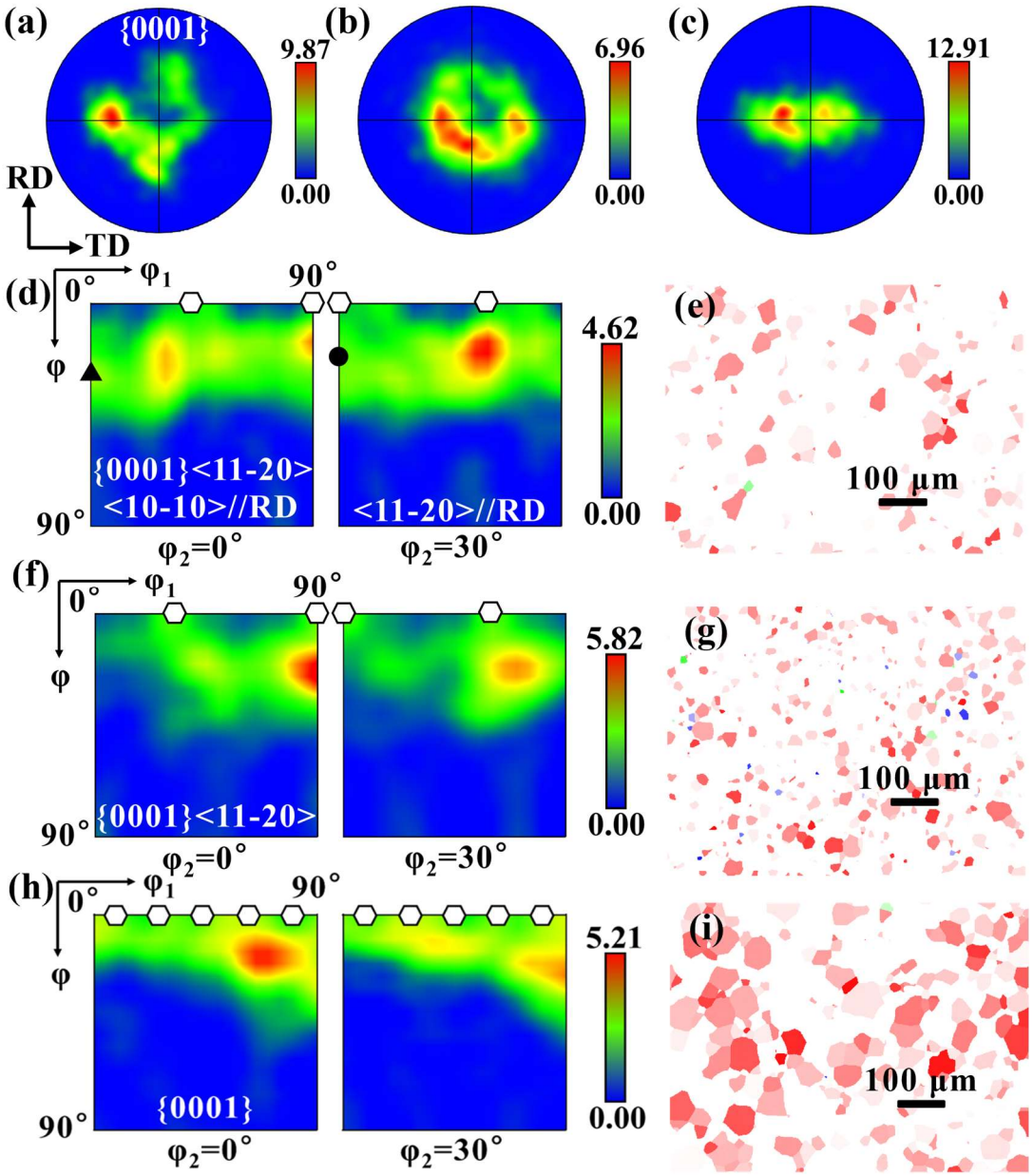


Figure 4. Pole figures, grain orientation maps, and IPF maps of annealed targets with different rolling directions: (a, d, e) 90° cross-rolled; (b, f, g) 45° cross-rolled; and (c, h, i) 0° (unidirectional) rolled. In the IPF maps, red represents <0001>//ND, green <10$\bar{1}$1>//ND, and blue <11$\bar{2}$0>//ND.

Grain orientation maps of annealed samples with different rolling directions are shown in Figure 4e,g, and i, and the content of each orientation is listed in Table 1. The annealed 90° rolled sample has a high proportion of red grains (16.7%), with only a few green grains and no blue grains, indicating that <0001>//ND is the dominant grain orientation. For the annealed 45° rolled sample, the proportion of red grains reaches 19.5%, acting as the predominant orientation. Moreover, the fraction of green grains increases slightly, and a small number of blue grains appear, though <0001>//ND remains the primary orientation of the annealed target under this rolling process. The proportion of <0001>//ND-oriented grains in the unidirectionally rolled annealed sample is 42.7%, which is far higher than that in the 90° and 45° rolled annealed samples. The rolling direction significantly affects the recrystallized texture composition after annealing by regulating grain rotation paths and stored energy distribution during deformation. Unidirectional rolling facilitates the formation of strong basal texture, whereas cross rolling effectively promotes orientation randomization.

Table 1. Content of each orientation in annealed targets with different rolling directions (%).

Target	90° rolled annealed target	45° rolled annealed target	0° rolled annealed target
<0001>//ND	16.7	19.5	42.7
$<10\bar{1}0>$//ND	0.13	0.18	0.08
$<11\bar{2}0>$//ND	0	0.45	0

Figure 5a–c presents BC maps of the annealed targets. All samples exhibit equiaxed grains and a relatively uniform internal contrast. The low KAM values (0.16°–0.24°) indicate that annealing substantially reduces the local orientation gradients. These microstructural features are consistent with extensive recovery and recrystallization. However, the available EBSD data do not enable continuous and discontinuous recrystallization to be unambiguously distinguished; therefore, no specific recrystallization mechanism was assigned in this study.

As shown in Figure 5d–f, the average grain sizes of the annealed 90°, 45°, and unidirectionally rolled targets are 25.50, 15.77, and 32.22 μm, respectively, while the corresponding maximum grain sizes are 53.69, 32.69, and 78.28 μm. To quantitatively evaluate grain-size uniformity, the grain-size distributions were fitted with a Gaussian function shown in Eq 1:

$$f(d) = A \times e^{-\frac{(d-d_0)^2}{2\sigma^2}} \quad (1)$$

where A is a constant, and d denotes a specific value, d_0 and σ represent the characteristic grain size and distribution width, respectively. The coefficient of variation was further calculated as coefficient of variation (CV) = $\sigma/d_0 \times 100\%$, and the fitting results are summarized in Figure 5g,h. The fitted σ values are 14.87 ± 2.35 μm for the 90° target, 5.95 ± 1.20 μm for the 45° target, and 26.31 ± 3.05 μm for the unidirectionally rolled target, corresponding to CV values of 58.31%, 37.73%, and 81.66%, respectively (Table 2). The 45° target exhibits the smallest σ and CV, indicating the narrowest and most concentrated grain-size distribution, whereas the unidirectionally rolled target has the largest values, indicating the widest distribution and a more pronounced coarse-grain tail. This conclusion is consistent with the maximum-to-average grain-size ratios of 2.11, 2.07, and 2.43 for the 90°, 45°, and unidirectionally rolled targets, respectively. Therefore, decreasing the rolling rotation angle from unidirectional rolling to 90° and then to 45° simultaneously promotes grain refinement and improves

grain-size uniformity, with the 45° target achieving the best combination of fine grains and a narrow size distribution.

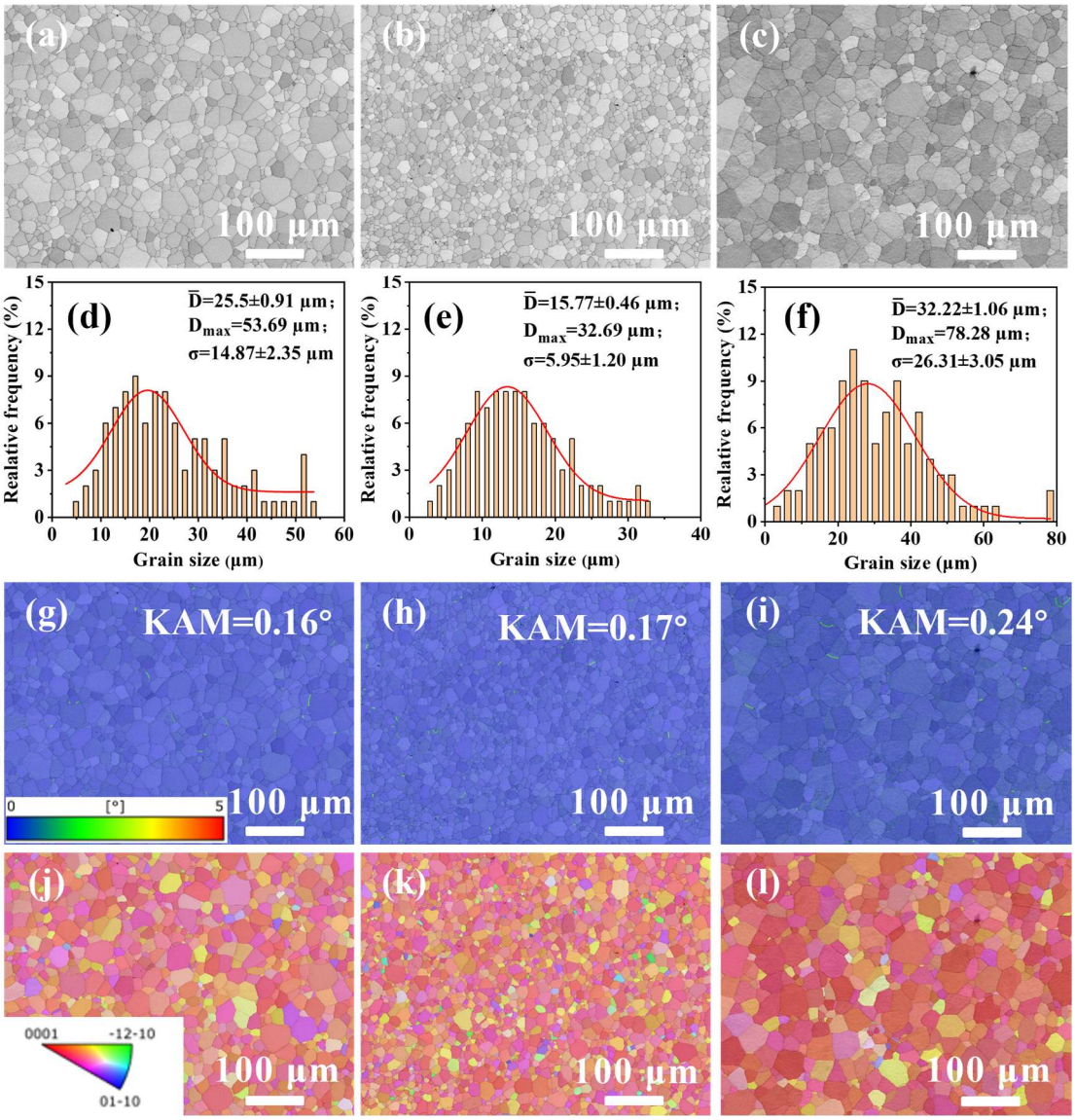


Figure 5. BC maps, grain size distribution maps, KAM maps, and IPF maps of annealed targets prepared under different rolling modes: (a, d, g, j) 90° cross-rolled annealed target; (b, e, h, k) 45° cross-rolled annealed target; and (c, f, i, l) 0° (unidirectionally) rolled annealed target.

Table 2. Average grain size, Gaussian distribution function σ, and normalization parameter CV (%) of the annealed samples.

Sample	d_0 (μm)	σ (μm)	CV (%)
90°rolled annealed target	25.50 ± 0.91	14.87 ± 2.35	58.31%
45° rolled annealed target	15.77 ± 0.46	5.95 ± 1.20	37.73%
0° rolled annealed target	32.22 ± 1.06	26.31 ± 3.05	81.66%

Figure 5g–l shows the KAM maps and IPF maps of the annealed targets with different rolling directions. According to the KAM maps (Figure 5g–i), the KAM values of the annealed 90° rolled sample and 45° rolled sample are 0.16° and 0.17°, respectively, while that of the unidirectionally rolled sample reaches 0.24°. KAM reflects local lattice misorientation and orientation gradients and does not directly quantify residual stress. Only alpha-Ti was indexed in the EBSD phase analysis, and grain boundaries were reconstructed using a 15° misorientation threshold; no interfaces were interpreted as phase boundaries. This indicates that the residual stresses in the 90° and 45° rolled samples are relatively low and uniformly distributed along the grain boundaries. The divergent trends of KAM and FWHM do not indicate inconsistent results because the two parameters describe different microstructural features. KAM reflects local orientation gradients, whereas FWHM is primarily sensitive to average microstrain and lattice-spacing heterogeneity. The unidirectionally rolled target exhibits the highest KAM but the narrowest peaks, while the 45° and 90° targets show lower, comparable KAM values but broader peaks, with the 90° target exhibiting the greatest broadening. These results indicate that local misorientation and average microstrain are complementary rather than monotonically correlated.

The IPF maps of the annealed targets with different rolling directions are displayed in Figure 5j–l, in which the crystallographic orientations of grains are represented by colors. Taking the 45° rolled annealed sample as a typical example, its grains are mainly red or reddish, accompanied by numerous grains with transitional colors (yellow and purple). Although the grain orientation is dominated by <0001>//ND, its proportion is notably lower than that of the unidirectionally rolled annealed sample. The two cross-rolled samples show little difference in orientation distribution: the 90° rolled annealed sample has almost no green and blue grains, while only a tiny number of green grains appear in the 45° rolled annealed sample. This result proves that the microstructure is more sufficiently fragmented, and the grain orientation becomes more uniform as the rolling rotation angle per pass decreases.

3.3. Surface morphology and properties of deposited thin films

The surface morphologies of the thin films deposited on samples with different rolling directions after annealing are illustrated in Figure 6a–c. These thin films were obtained by a single-run deposition. No large detached particles are deposited on the film surfaces, nor are there any obvious voids. The films are relatively smooth and compact, indicating that although cross rolling can enhance the degree of grain fragmentation, the internal stored energy does not increase significantly. For the target annealed at 600 ℃ for 1 h, the residual stress during sputtering is insufficient to trigger the initiation and propagation of microcracks; hence, no large particles are deposited on the film surfaces.

As shown in Figure 6d–f, the films deposited using the 90°, unidirectionally rolled, and 45° annealed targets have thicknesses of 313.9, 353.9, and 440.5 nm, respectively, corresponding to deposition rates of 15.70, 17.70, and 22.02 nm/min, respectively. The deposition rate does not vary monotonically with the {0001}//ND fraction. Although the 90° target has the lowest basal fraction (16.7%), its film shows the lowest deposition rate. Compared with the 45° target, it has coarser and less uniform grains and the strongest XRD peak broadening, indicating a higher level of residual lattice distortion. These adverse effects outweigh the benefit of texture weakening. In contrast, the 45° target combines the finest characteristic grain size, the smallest σ and CV, and a moderate basal fraction (19.5%). Its enhanced grain-boundary density and improved uniformity stabilize the local sputtering process and compensate for the reduced basal texture, resulting in the highest deposition rate. The unidirectionally

rolled target has the strongest basal texture (42.7%) and the narrowest XRD peaks, but its coarse grains and broad size distribution lead to an intermediate deposition rate. Therefore, the deposition rate is governed by the coupled effects of grain size, grain-size uniformity, texture, and residual lattice distortion rather than by texture alone. Consistent with the experimental results reported by Yu [15], refined-grain targets exhibit significantly higher sputtering yields under identical process conditions.

To further investigate the surface quality of the thin films, AFM characterization was carried out on the films deposited by annealed targets with different rolling directions, and the results are shown in Figure 6g–i. It can be observed from the AFM images that there are numerous protrusions and depressions on the film surfaces, leading to relatively large surface undulation. The annealed unidirectionally rolled target yields the deposited film with the minimum surface roughness: R_a = 3.02 nm and R_q = 3.82 nm (R_a: arithmetic average roughness; R_q: root-mean-square roughness). The surface roughness values R_a of the films deposited by the 90° rolled and 45° rolled annealed targets are 4.42 and 6.85 nm, respectively, with the corresponding R_q values being 5.7 and 8.65 nm. It is clear that the surface roughness of the films deposited by the annealed targets shows an upward trend in the sequence from the unidirectional rolling to 45° rolling and 90° rolling.

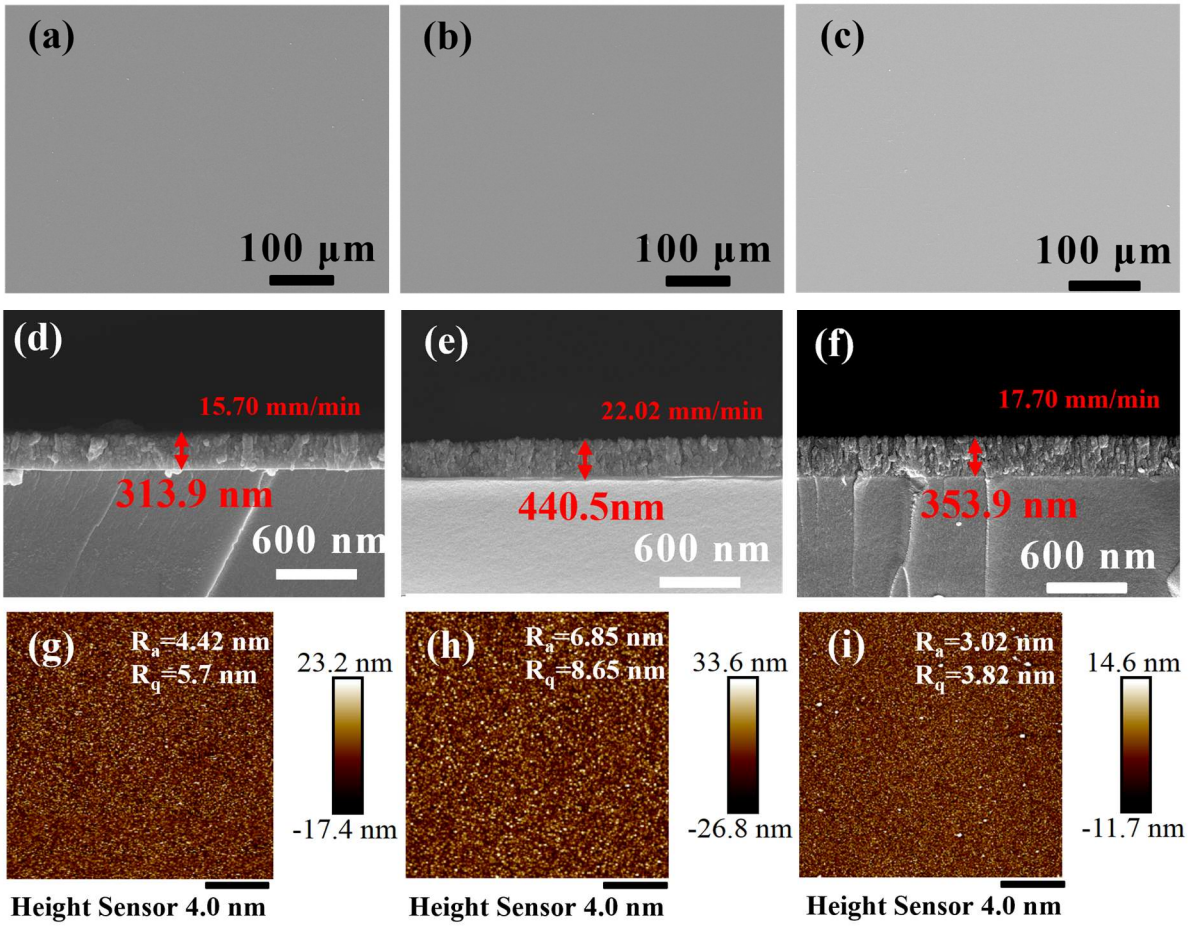


Figure 6. Surface, cross-sectional and AFM morphologies of thin films from annealed targets with different rolling directions. (a–c) Top-view SEM; (d–f) cross-sectional SEM; (g–i) 2D AFM. (a, d, g) 90° rolled; (b, e, h) 45° rolled; and (c, f, i) 0° (unidirectional) rolled annealed targets.

The variation in the surface roughness of the thin films is dominated by the texture characteristics and grain uniformity of the sputtering targets. It is worth noting that all the as-deposited thin films exhibit ultra-low surface roughness at the nanometer scale, indicating excellent surface quality overall. Under the same annealing conditions, the unidirectionally rolled annealed target possesses an extremely strong {0001} basal texture with an orientation fraction of 42.7%, where the c-axes of grains are highly parallel to the normal direction. In comparison, the {0001} texture contents of the 90° and 45° rolled annealed targets are only 16.7% and 19.5%, and their more dispersed orientations can promote orientation-dependent nucleation and growth, leading to higher R_a values of 4.42 and 6.85 nm, respectively. Large sputtering-rate differences and lower grain uniformity produce minor microscopic undulations on the film surface [12,16]. Notably, the 45°-rolled target possesses the smallest σ and CV; the most uniform grain-size distribution. Its higher film roughness therefore does not stem from grain inhomogeneity. With the highest deposition rate and thickest film (440.5 nm), it shortens adatom diffusion time, promoting kinetic roughening and surface-undulation accumulation. These results indicate that film roughness is controlled by the coupled effects of target texture, deposition flux, film thickness, and growth kinetics, while grain-size uniformity mainly stabilizes the local sputtering flux and does not exhibit a simple monotonic relationship with film roughness.

4. Conclusions

In this work, the grain size and {0001} texture of titanium targets were effectively regulated by adjusting the rolling angle, and the intrinsic relationship between the target microstructure and thin-film sputtering performance was established. Under the 45° cross-rolling process, a high-purity titanium target with an average grain size of 15.77 μm was successfully prepared, increasing the sputtering rate from 15.70 to 22.02 nm/min. The main conclusions are as follows:

1. After annealing, the characteristic grain size decreased from 32.22 to 25.50 and 15.77 μm as the rolling mode changed from unidirectional rolling to 90° and then to 45° rolling, respectively. The corresponding Gaussian distribution width σ decreased from 26.31 to 14.87 and 5.95 μm, while the coefficient of variation CV decreased from 81.66% to 58.31% and 37.73%, respectively. These results demonstrate that the 45° rolled annealed target achieved the finest grains and the narrowest, most uniform grain-size distribution.

2. Reducing the rolling rotation angle effectively weakened the {0001} basal texture and facilitated the randomization of grain orientations. The unidirectionally rolled and annealed target exhibited the highest <0001>//ND orientation fraction, reaching 42.7%, whereas this fraction decreased to 16.7% and 19.5% for the 90° and 45° cross-rolled annealed specimens, respectively. Multi-directional rolling promoted a more dispersed grain-orientation distribution by modifying the strain path, but texture alone did not determine the final deposition behavior.

3. The Ti films were dense with ultra-low surface roughness. Although changing the rolling direction slightly increased roughness, all films maintained excellent surface quality (R_a: 3.02–6.85 nm). The 45° rolled and annealed target achieved the highest deposition rate of 22.02 nm/min, mainly owing to its fine and uniform grain structure rather than basal texture alone, indicating a trade-off between improved deposition efficiency and increased film roughness.

Use of AI tools declaration

The authors declare they have not used Artificial Intelligence (AI) tools in the creation of this article.

Author contributions

Kewen Zhao: Writing-original draft, investigation, conceptualization; Zhipeng Song: supervision, investigation, conceptualization; Hongjun Yuan: supervision, conceptualization; Wei Zhang: supervision; Juanjuan Wang: supervision; Junbao Guo: supervision; Longzhen Zhang: writing–review & editing, supervision, resources; Chengyu Hu: resources; Gequan Hu: resources; Xiaochao Wu: resources; Qingkui Li: resources, funding acquisition; Jilin He: resources.

Funding

The Key R&D Program of Henan Province, No. 261111230300, Longzhen Zhang, the Project of Ningxia Horizontal Titanium Industry Co., Ltd. Grant, No. KT2024Z05, Hongjun Yuan, the Project of Zhongyuan Critical Metals Laboratory, No. GJJSCXPT202401, Longzhen Zhang.

Acknowledgments

This work was supported by the Key R&D Program of Henan Province (No. 261111230300), the Project of Ningxia Horizontal Titanium Industry Co., Ltd. (Grant No. KT2024Z05), and the Project of Zhongyuan Critical Metals Laboratory (No. GJJSCXPT202401), Zhengzhou University, China.

Conflict of interest

The authors declare no conflict of interest.

References

1. Geetha M, Singh AK, Asokamani R, et al. (2009) Ti based biomaterials, the ultimate choice for orthopaedic implants—A review. *Prog Mater Sci* 54: 397–425. https://doi.org/10.1016/j.pmatsci.2008.06.004
2. Deng B, Ye T, Guo D (2012) Effects of vanadium ion implantation on microstructure, mechanical and tribological properties of TiN coatings. *Appl Surf Sci* 258: 9080–9086. https://doi.org/10.1016/J.APSUSC.2012.06.001
3. Xu GH, Zhao XB, Xia WS, et al. (2025) A review on microstructure design, processing, and strengthening mechanism of high-strength titanium alloys. *Prog Nat Sci Mater Int* 35: 258–277. https://doi.org/10.1016/j.pnsc.2025.01.005
4. Thakur VK, Vennerberg D, Kessler MR (2014) Green aqueous surface modification of polypropylene for novel polymer nanocomposites. *ACS Appl Mater Interfaces* 6: 9349–9356. https://doi.org/10.1021/am501726d

5. Li CH, Liu KR, Wei SC, et al. (2023) Research progress on titanium nitride thin films fabricated by magnetron sputtering. *Mater Prot* 56: 111–119. https://doi.org/10.16577/j.issn.1001-1560.2023.0041
6. Gao WN, Liu SL, Dang P, et al. (2014) Preparation process of titanium targets for sputter coating. *Heat Treat Met* 39: 43–46. https://link.cnki.net/doi/10.13251/j.issn.0254-6051.2014.12.010
7. Nguyen QD, Phan QD, Quy TĐ, et al. (2019) Effects of Ti target poisoning to titanium nitride coating fabricated by a physical vapor deposition technique. *Appl Mech Mater* 889: 185–189. https://doi.org/10.4028/www.scientific.net/AMM.889.185
8. Liu L, Li W, Sun H, et al. (2022) Effects of Ti target purity and microstructure on deposition rate, microstructure and properties of Ti films. *Materials* 15: 2661. https://doi.org/10.3390/ma15072661
9. Wu BH, Yu Y, Wu J, et al. (2018) Tailoring of titanium thin film properties in high power pulsed magnetron sputtering. *Vacuum* 150: 144–154. https://doi.org/10.1016/j.vacuum.2018.01.014
10. Moskovkin P, Maszl C, Schierholz R, et al. (2021) Link between plasma properties with morphological, structural and mechanical properties of thin Ti films deposited by high power impulse magnetron sputtering. *Surf Coat Tech* 418: 127235. https://doi.org/10.1016/j.surfcoat.2021.127235
11. Zhu Q, Wang L, Yang QL, et al. (2014) Extrusion theory and microstructure-property analysis of molybdenum tube targets. *China Molybdenum Ind* 38: 50–53. Available from: https://zgmy.cbpt.cnki.net/portal/journal/portal/client/paper/5e4fde1722dec04942b4dbd16b98bde2
12. Zhang X, Zhu Q, Zheng M, et al. (2025) Localized high-temperature laser shock peening with adjustable metallic coatings method for mechanical properties enhancement of reflective aluminum alloys. *J Mater Process Technol* 338: 118792. https://doi.org/10.1016/j.jmatprotec.2025.118792
13. Song RX, Wang D, Yang C, et al. (2025) A review of grain refinement and texture engineering in aluminum alloy magnetron sputtering targets. *Materials* 18: 3235. https://doi.org/10.3390/ma18143235
14. Zhang L, Li XY, Qu XH, et al. (2022) Powder metallurgy route to ultrafine-grained refractory metals. *Adv Mater* 35: 2205807. https://doi.org/10.1002/adma.202205807
15. Yu K, Xue X, Xu L, et al. (2024) Effect of grain size and orientation on magnetron sputtering yield of tantalum. *Int J Refract Met Hard Mater* 126: 106948. https://doi.org/10.1016/j.ijrmhm.2024.106948
16. Solonenko OP, Ando Y, Nishiyama H, et al. (2018) Synthesis of thick photocatalytic titania surface layers by solution plasma spraying and subsequent treatment by pulsed laminar plasma jet. *Surf Coat Tech* 333: 39–51. https://doi.org/10.1016/j.surfcoat.2017.10.064



AIMS Press

© 2026 the Author(s), licensee AIMS Press. This is an open access article distributed under the terms of the Creative Commons Attribution License (http://creativecommons.org/licenses/by/4.0)